The Astrophysical Journal, 687:608–622, 2008 November 1

COLLISIONAL AND THERMAL EMISSION MODELS OF DEBRIS DISKS: TOWARD PLANETESIMAL POPULATION PROPERTIES

Alexander V. Krivov, Sebastian Müller, Torsten Löhne, and Harald Mutschke
Astrophysikalisches Institut und Universitätssternwarte, Friedrich Schiller University Jena,
Schillergäßchen 2–3, 07745 Jena, Germany; krivov@astro.uni-jena.de
Received 2008 May 21; accepted 2008 July 2

ABSTRACT

Debris disks around main-sequence stars are believed to derive from planetesimal populations that have accreted at early epochs and survived possible planet formation processes. While debris disks must contain solids in a broad range of sizes—from big planetesimals down to tiny dust grains—debris disk observations are only sensitive to the dust end of the size distribution. Collisional models of debris disks are needed to "climb up" the ladder of the collisional cascade, from dust toward parent bodies, representing the main mass reservoir of the disks. We have used our collisional code to generate five disks around a Sun-like star, assuming planetesimal belts at 3, 10, 30, 100, and 200 AU with 10 times the Edgeworth-Kuiper Belt mass density, and to evolve them for 10 Gyr. Along with an appropriate scaling rule, this effectively yields a three-parametric set of reference disks (initial mass, location of planetesimal belt, and age). For all the disks, we have generated spectral energy distributions (SEDs), assuming homogeneous spherical astrosilicate dust grains. A comparison between generated and actually observed SEDs yields estimates of planetesimal properties (location, total mass, etc.). As a test and a first application of this approach, we have selected five disks around Sun-like stars with well-known SEDs. In four cases, we have reproduced the data with a linear combination of two disks from the grid (an "asteroid belt" at 3 AU and an outer "Kuiper Belt"); in one case a single, outer component was sufficient. The outer components are compatible with "large Kuiper Belts" of 0.2–50 Earth masses (in bodies up to 100 km in size) with radii of 100–200 AU.

Subject headings: circumstellar matter — planetary systems: formation — Kuiper Belt — stars: individual (HD 377, HD 70573, HD 72905, HD 107146, HD 141943)

1. INTRODUCTION

Since the *IRAS* discovery of the excess infrared emission around Vega by Aumann et al. (1984), infrared surveys with *IRAS*, *ISO*, *Spitzer*, and other space-based and ground-based telescopes have shown the Vega phenomenon to be common for main-sequence stars (e.g., Meyer et al. 2004; Beichman et al. 2005; Najita & Williams 2005; Rieke et al. 2005; Bryden et al. 2006; Siegler et al. 2007; Su et al. 2006; Trilling et al. 2007, 2008; Hillenbrand et al. 2008). The observed excesses are attributed to circumstellar disks of second-generation dust, sustained by numerous planetesimals in orbit around the stars. Jostling collisions between planetesimals grind them all the way down to smallest dust grains which are then blown away by stellar radiation. While the bulk of such a debris disk's mass is hidden in invisible parent bodies, the observed luminosity is dominated by small particles at dust sizes. Hence, the studies of dust emission have the potential to shed light onto the properties of parent planetesimal populations, as well as planets that may shape them, and, ultimately, onto the evolutionary history of circumstellar planetary systems.

However, there is no direct way to infer the properties of invisible planetesimal populations from the observed dust emission. Dust and planetesimals can only be linked through models. First, dynamical models can be used to predict, for a given planetesimal family (mass, location, age, etc.), the distribution of dust. Such models have become available in recent years (e.g., Thébault et al. 2003; Krivov et al. 2006; Thébault & Augereau 2007; Wyatt et al. 2007; Löhne et al. 2008). After that, standard thermal emission models will describe the resulting dust emission. Comparison of that emission to the one actually observed would then reveal the probable properties of underlying, dust-producing planetesimal families.

In this paper we follow this approach and generate a set of hypothetical debris disks around G2 dwarfs with different ages (10 Myr–10 Gyr), assuming debris dust to stem from planetesimal belts with different initial masses at different distances from the central star. For every set of these parameters, we simulate steady-state dust distributions with our collisional code (Krivov et al. 2005, 2006; Löhne et al. 2008). This is different from a traditional, "empirical" approach, in which dust distributions are postulated, usually in form of power laws, parameterized by ranges and exponents that play the role of fitting parameters (e.g., Wolf & Hillenbrand 2003). Interestingly, replacing formal dust distributions with those coming out of dynamical modeling does not increase the number of fitting parameters. Just the opposite: the number of parameters reduces and those parameters that we keep free all have clear astrophysical meaning. The most important are the location of the parent planetesimal belt and its current mass (Wyatt et al. 2007).

Having produced a set of model debris disks, we compute thermal emission fluxes in a wide range of wavelengths from mid-infrared to millimeter. In so doing, we completely abandon simple blackbody or modified blackbody calculations and solve a thermal balance equation instead. At this stage, we assume compact spherical grains composed of astronomical silicate (Laor & Draine 1993) and employ standard Mie calculations to compute dust opacities. Although this is still a noticeable simplification, it represents a natural step toward considering realistic materials and using more involved methods of light-scattering theory that we leave for subsequent papers.

As a test and a first application of the results, we reinterprete available observational data on a selection of disks around Sun-like stars with well-known spectral energy distributions (SEDs).

This paper is organized as follows. Section 2 describes the dynamical and thermal emission models. In § 3 a set of reference

disks is introduced and the model parameters are specified. Section 4 presents the modeling results for this set of disks: size and spatial distribution of dust, dust temperatures, and the generated SEDs. Application to selected observed disks is made in § 5. Section 6 summarizes the paper.

2. MODEL

2.1. *Dynamical Model*

To simulate the dust production by the planetesimal belt and the dynamical evolution of a disk, we use our collisional code (ACE [Analysis of Collisional Evolution]). The code numerically solves the Boltzmann-Smoluchowski kinetic equation to evolve a disk of solids in a broad range of sizes (from smallest dust grains to planetesimals), orbiting a primary in nearly Keplerian orbits (gravity + direct radiation pressure + drag forces) and experiencing disruptive and erosive (cratering) collisions. Collision outcomes are simulated with available material- and size-dependent scaling laws for fragmentation and dispersal in both strength and gravity regime. The current version implements a three-dimensional kinetic model, with masses, semimajor axes, and eccentricities as phase-space variables. This approach automatically enables a study of the simultaneous evolution of mass, spatial, and velocity distribution of particles. The code is fast enough to easily follow the evolution of a debris disk over gigayear timescales. A detailed description of our approach, its numerical implementation, and astrophysical applications can be found in our previous papers (Krivov et al. 2000, 2005, 2006; Löhne et al. 2008).

2.2. *Thermal Emission Model*

For spherical dust grains with radius s and temperature T_g we can calculate their distance r to the star under the assumption of thermal equilibrium as

$$r = \frac{R_*}{2}\sqrt{\frac{\int_0^\infty d\lambda Q_\lambda^{\rm abs}(s) F_{\lambda,*}(T_*)}{\int_0^\infty d\lambda Q_\lambda^{\rm abs}(s) B_\lambda(T_g)}}. \quad (1)$$

Here R_* denotes the radius, $F_{\lambda,*}(T_*)$ the flux of the star with an effective temperature T_*, and $B_\lambda(T_g)$ the Planck function. The absorption efficiency $Q_\lambda^{\rm abs}(s)$ is a function of wavelength λ and particle size.

We now consider a rotationally symmetric dust disk at a distance D from the observer. Denote by $N(r, s)$ the surface number density of grains with radius s at a distance r from the star, so that $N(r, s)ds$ is the number of grains with radii $[s, s + ds]$ in a narrow annulus of radius r, divided by the surface area of that annulus. Then the specific flux emitted from the entire disk at a given wavelength can be calculated as

$$F_{\lambda,\rm disk}^{\rm tot} = \int dr \int ds\, F_{\lambda,\rm disk}(r, s) \quad (2)$$

$$= \frac{2\pi^2}{D^2}\int dT_g\, r(T_g)\frac{dr(T_g)}{dT_g}\int ds\, s^2 \times N(r, s) Q_\lambda^{\rm abs}(s) B_\lambda(T_g). \quad (3)$$

3. REFERENCE DISKS

3.1. *Central Star*

The parameters of the central star (mass and photospheric spectrum) affect both the dynamics of solids (by setting the scale of orbital velocities and determining the radiation pressure strength) and their thermal emission (by setting the dust grain temperatures). We take the Sun (a G2 V dwarf with a solar metallicity) as a central star and calculate its photospheric spectrum with the NextGen grid of models (Hauschildt et al. 1999).

3.2. *Forces*

In the dynamical model, we include central star's gravity and direct radiation pressure. We switch off the drag forces (both the Poynting-Robertson and stellar wind drag), which are of little importance for the optical depths in the range from $\sim 10^{-5}$ to $\sim 10^{-3}$) considered here (Artymowicz 1997; Krivov et al. 2000; Wyatt 2005).

3.3. *Collisions*

The radii of solids in every modeled disk cover the interval from 0.1 μm to 100 km. The upper limit of 100 km is justified by the fact that planetesimal accretion models predict larger objects to have a steeper size distribution and thus to contribute less to the mass budget of a debris disk (e.g., Kenyon & Luu 1999b). To describe the collisional outcomes, we make the same assumptions as in Löhne et al. (2008). This applies, in particular, to the critical energy for disruption and dispersal, $Q_D^*(s)$, as well as to the size distribution of fragments of an individual collision. However, in contrast to Löhne et al. (2008), where only catastrophic collisions were taken into account, we include here cratering collisions as well. This is necessary, as cratering collisions alter the size distribution of dust in the disk markedly, which shows up in the SEDs (Thébault et al. 2003; Thébault & Augereau 2007). The actual model of cratering collisions used here is close to that by Thébault & Augereau (2007). An essential difference is our assumption of a single power law for the size distribution of the fragments of an individual collision instead of the broken power law proposed originally in Thébault et al. (2003). However, this difference has little effect on the resulting size distribution in collisional equilibrium.

3.4. *Optical Properties of Dust*

An important issue is a choice of grain composition and morphology. These affect both the dynamical model (through radiation pressure efficiency as well as bulk density) and thermal emission model (through absorption efficiency). Here we assume compact spherical grains composed of astronomical silicate (aka astrosilicate or astrosil; Laor & Draine 1993), similar to the $MgFeSiO_4$ olivine, with a density of 3.3 g cm^{-3}. Taking optical constants from Laor & Draine (1993) we calculated radiation pressure efficiency $Q_{\rm pr}$ and absorption efficiency $Q_{\rm abs}$ with a standard Mie routine (Bohren & Huffman 1983).

To characterize the radiation pressure strength, it is customary to use the radiation pressure to gravity ratio β (Burns et al. 1979), which is independent of distance from the star and, for a given star, only depends on $Q_{\rm pr}$ and particle size. If grains that are small enough to respond to radiation pressure derive from collisions of larger objects in nearly circular orbits, they will get in orbits with eccentricities $e \sim \beta/(1 - \beta)$. This implies that grains with $\beta < 0.5$ remain orbiting the star, whereas those with $\beta > 0.5$ leave the system in hyperbolic orbits. The β ratio for compact astrosil grains, computed from $Q_{\rm pr}$, is shown in Figure 1. The blowout limit, $\beta = 0.5$, corresponds to the grain radius of $s = 0.4$ μm. Note that the tiniest astrosil grains ($\lesssim 0.1$ μm) would have $\beta < 0.5$ again and thus could orbit the star in bound orbits. However, the dynamics of these small motes would be subject to a variety of effects (e.g., the Lorentz force) not included in our model, and their lifetimes may be shortened by erosion processes (e.g., stellar wind sputtering). Altogether, we expect them to make little contribution

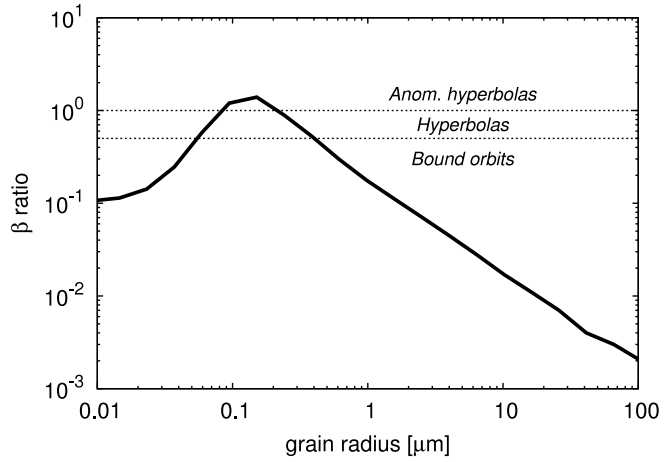

FIG. 1.—Radiation pressure to gravity ratio β for astrosilicate grains as a function of their size. Horizontal lines at $\beta = 0.5$ and 1.0 show which particles typically move in bound elliptic orbits, in hyperbolas, as well as in anomalous hyperbolas (open outward from the star).

to the thermal emission in the mid-IR to submillimeter. By setting the minimum radius of grains to 0.1 μm, we therefore do not take into account these grains here.

The spectral dependence of the absorption efficiency $Q_{\rm abs}$ of different-sized astrosil spheres is depicted in Figure 2.

3.5. *Parent Planetesimal Belts*

To have a representative set of "reference" debris disks around Sun-like stars, we consider possible planetesimal rings centered at the semimajor axes of $a = 3$, 10, 30, 100, and 200 AU from the primary. All five rings are assumed to have the same relative width initially (again, in terms of semimajor axis) of $\Delta a/a = 0.2$ (± 0.1) and share the same semiopening angle (the same as the maximum orbital inclination of the objects) of $\varepsilon = 0.1$ rad. The orbital eccentricities of planetesimals are then distributed uniformly between 0.0 and 0.2, in accordance with the standard equipartition condition. The initial (differential) mass distribution of all solids is given by a power law with the index 1.87, a value that accounts for the modification of the classical Dohnanyi's (1969) 1.833 through the size dependence of material strength (see, e.g., Durda & Dermott 1997).

The initial disk mass is taken to be 1 $M_\oplus$ (Earth mass) for a 30 AU ring, roughly corresponding to 10 (or slightly more) times the Edgeworth-Kuiper Belt (EKB) mass (e.g., Gladman et al. 2001; Hahn & Malhotra 2005). For other parent ring locations, the initial mass is taken in such a way as to provide approximately the same spatial *density* of material. Since the circumference of a ring $2\pi a$, its absolute width Δa, and its vertical thickness $2a\varepsilon$ are all proportional to a, the condition of a constant density requires the mass scaling $\propto a^3$. This corresponds to the initial mass ranging from $\approx 0.001\ M_\oplus$ in the 3 AU case to $\approx 200\ M_\oplus$ in the 200 AU case. With these values, all reference disks have about 10 times the EKB density (10 EKBD).

That all the belts share the same volume density of material is purely a matter of convention. Instead, we could choose them to have the same surface density or the same total mass. Given the scaling rules, as discussed in the text and Appendix A, none of these choices would have strong advantages or disadvantages.

All five reference disks are listed in Table 1. We evolved them with the collisional code, ACE, and stored all results between the ages of 10 Myr and 10 Gyr at reasonable time steps. In what follows, we use self-explanatory identifiers like 10EKBD at 10 AU at 300 Myr to refer to a particular disk of a particular age.

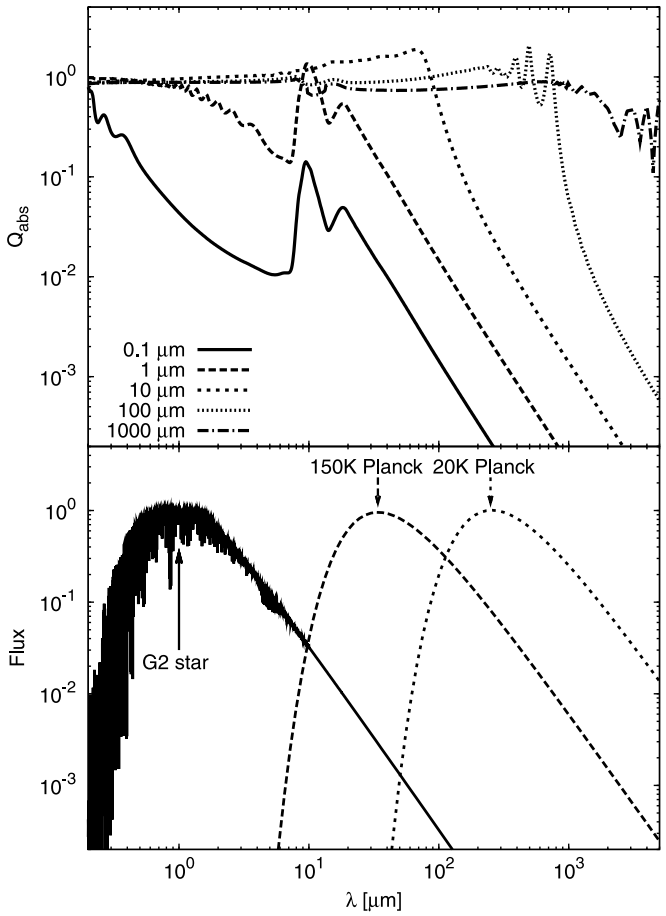

FIG. 2.—*Top*: Absorption efficiency of astrosilicate compact spherical grains as a function of wavelength for different grain sizes. *Bottom*: Spectrum of a G2 V star and the Planck curves for 150 and 20 K (in arbitrary vertical scale) to indicate the spectral ranges most important for absorption and emission.

Importantly, the same runs of the collisional code automatically provide the results for disks of any other initial density (or mass). This is possible due to the mass-time scaling of Löhne et al. (2008), which can be formulated as follows. Denote by $M(M_0, t)$ the mass that a disk with initial mass M_0 has at time t. Then, the mass of another disk with x times larger initial mass at time instant t/x is simply

$$M(xM_0, t/x) = xM(M_0, t). \tag{4}$$

For instance, the mass of the 1EKBD at 10 AU at 10 Gyr disk is one-tenth of the 10EKBD at 10 AU at 1 Gyr disk mass. Note that the same scaling applies to any other quantity directly proportional to the amount of disk material. In other words, M may equally stand for the mass of dust, its total cross section, thermal radiation flux, etc. See Appendix A for additional explanations.

4. RESULTS

4.1. *Size and Spatial Distributions of Dust*

As noted above, the collisional code ACE uses masses and orbital elements of disk particles as phase-space variables. At any time instant, their phase-space distribution is transformed to usual mass/size and spatial distributions. It is important to understand that mass/size distributions and spatial distributions cannot, generally, be decoupled from each other. Grains of different sizes have different radial distributions and, conversely, the size distribution of material is different at different distances from the star.

TABLE 1
Description of Reference Disks

Disk Identifier	Belt Location (AU)	Initial Disk Mass ($M_\oplus$)	a Range (AU)	r Range (AU)
10EKBD at 3 AU	3	0.001	0.3–30	0.5–20
10EKBD at 10 AU	10	0.03	1–100	2–50
10EKBD at 30 AU	30	1	3–300	5–200
10EKBD at 100 AU	100	30	10–1000	20–500
10EKBD at 200 AU	200	200	20–2000	30–1000

A typical size distribution of solids is shown in Figure 3 for one of the disks, namely, 10EKBD at 30 AU at 100 Myr. Different lines correspond to different distances from the primary. As expected, the size distribution is the broadest within the parent ring of planetesimals. Farther out, it only contains grains which are small enough to develop orbits with sufficiently large apocentric distances due to radiation pressure.

The spatial distribution of material in the same disk is shown in Figure 4. Here, different lines refer to different particle sizes. The ring of the biggest particles shown (100 μm), for which radiation pressure is negligible, nearly coincides with the initial ring of planetesimals (semimajor axes from 27 to 33 AU, eccentricities from 0.0 to 0.2, and hence radial distances from 22 to 40 AU). The larger the particles, the more confined their rings. The rings are more extended outward with respect to the parent planetesimal ring than inward.

Radial profiles of the normal geometrical optical depth for three reference disks (planetesimal rings at 10, 30, and 100 AU) are depicted in Figure 5. Initially, the peak optical depth of the disks is proportional to the distance of the parent ring, making the 100 AU disk 10 times optically thicker than the 10 AU one. The subsequent collisional evolution of the disks depends on their initial mass and distance from the star, as explained in detail in Löhne et al. (2008) and Appendix A. Once a collisional steady state is reached (which is the case after 10 Myr for all three disks), the optical depth decays with time approximately as $t^{-\xi}$, where $\xi \approx 0.3...0.4$, i.e., roughly by 1 order of magnitude from 10 Myr to 10 Gyr. In a steady-state regime, the optical depth is proportional to $r^{1+1.3\xi} \sim r^{1.5}$. This explains why, at any age between 10 Myr and 10 Gyr, the 100 AU ring is ≈30 times optically thicker than the 10 AU one.

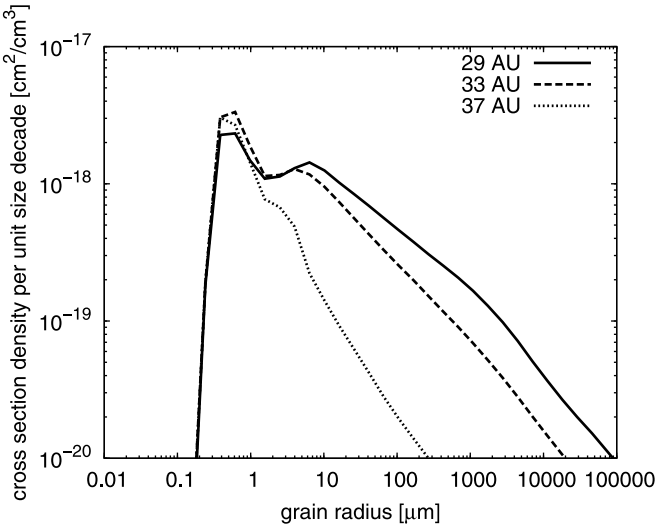

Fig. 3.—Size distribution in the 10EKBD at 30 AU at 100 Myr disk at three different distances from the star.

4.2. *Dust Temperatures*

Figure 6 shows the dust temperatures as a function of two variables: grain distances from the star and their radii. In a parallel scale on the right, we show typical size distributions (cf. Fig. 3). Similarly, under the temperature plot, typical radial profiles of the disk are drawn (cf. Fig. 4). This enables a direct "read-out" of the typical[1] temperature in one or another disk. We find, for example, 130 K at 10 AU, 90 K at 30 AU, and 50 K at 100 AU.

These values are noticeably higher than the blackbody values of 88, 51, and 28 K, respectively. The reason for these big deviations and for the S-shaped isotherms in Figure 6 is the astronomical silicate's spectroscopic properties with relatively high absorption at visible wavelengths and steeply decreasing absorption coefficient at longer wavelengths (see Fig. 2). The cross section–dominating astrosil grains are in a size range where the absorption efficiency for visible and near-infrared wavelengths (around 1 μm) has already reached the blackbody value, while emission is still rather inefficient. With the enhancement of the emission efficiencies relative to the "saturated" absorption, temperatures drop drastically for somewhat larger grains. The larger the distance from the star (yielding lower average temperature

[1] "Typical" in the sense that it is the temperature of cross-section dominating grains in the densest part of the disk.

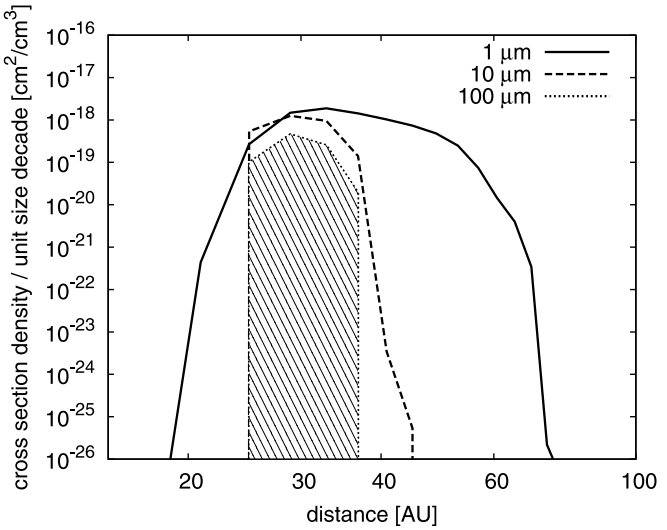

Fig. 4.—Spatial distribution of grains with three characteristic radii for the 10EKBD at 30 AU at 100 Myr disk. The ring of the biggest particles shown (100 μm, *shaded area*) is the narrowest. Its radial extension is nearly the same as that of the initial planetesimal ring; vertical "walls" are artifacts due to a discrete distance binning.

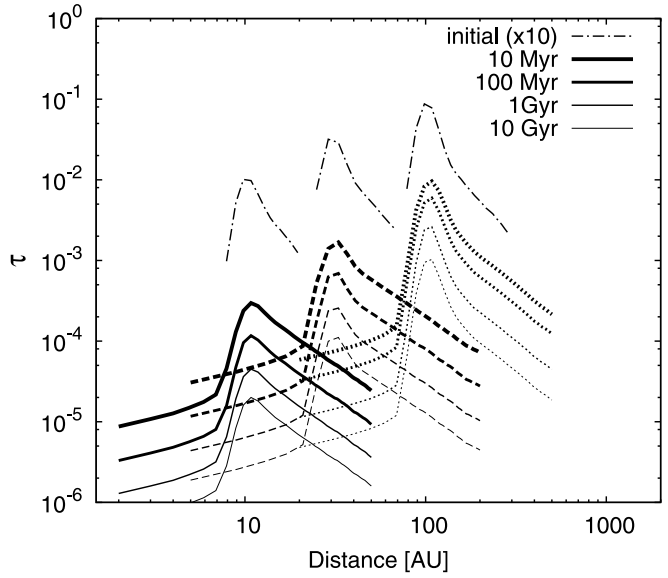

FIG. 5.—Radial profiles of the normal geometrical optical depth for three out of five basic runs (10EKBD at 10 AU, *solid lines*; 10EKBD at 30 AU, *dashed lines*; 10EKBD at 100 AU, *dotted lines*) at different ages. The thinner the line, the older the disk, as marked in the legend. The dash-dotted lines are initial optical depths, artificially enhanced by a factor of 10 for better visibility.

and lower emission efficiency), the wider the size range over which the temperature decreases, and the stronger the temperature difference between small and large grains. This explains why the S shape of the isotherms gets more pronounced from the left to the right in Figure 6.

Furthermore, we note that Mie resonances can increase the absorption/emission efficiencies even beyond unity for wavelengths somewhat longer than the grain size (see 1, 10, and 100 μm curves in Fig. 2). This explains the temperature maximum for grains of about 0.3 μm radius ("resonance" with the stellar radiation maximum) and the minimum with temperatures even below the blackbody values for 10–50 μm grain radius ("resonance" with the blackbody emission peak).

4.3. *Spectral Energy Distributions*

We start with a single, "typical" SED for one of the disks. Such an SED for the 1EKBD at 30 AU at 100 Myr disk is shown in Figure 7 with a thick solid line. It peaks at about 50 μm, which is consistent with the dust temperatures (Fig. 6). The hump at $\approx$10 μm is due to a classical silicate feature, as discussed below.

For comparison, we have overplotted the SEDs calculated for the same disk, but under different assumptions about the absorbing and emitting properties of grains: in a blackbody approximation (*gray line*) and for amorphous carbon (*dashed line*). Note

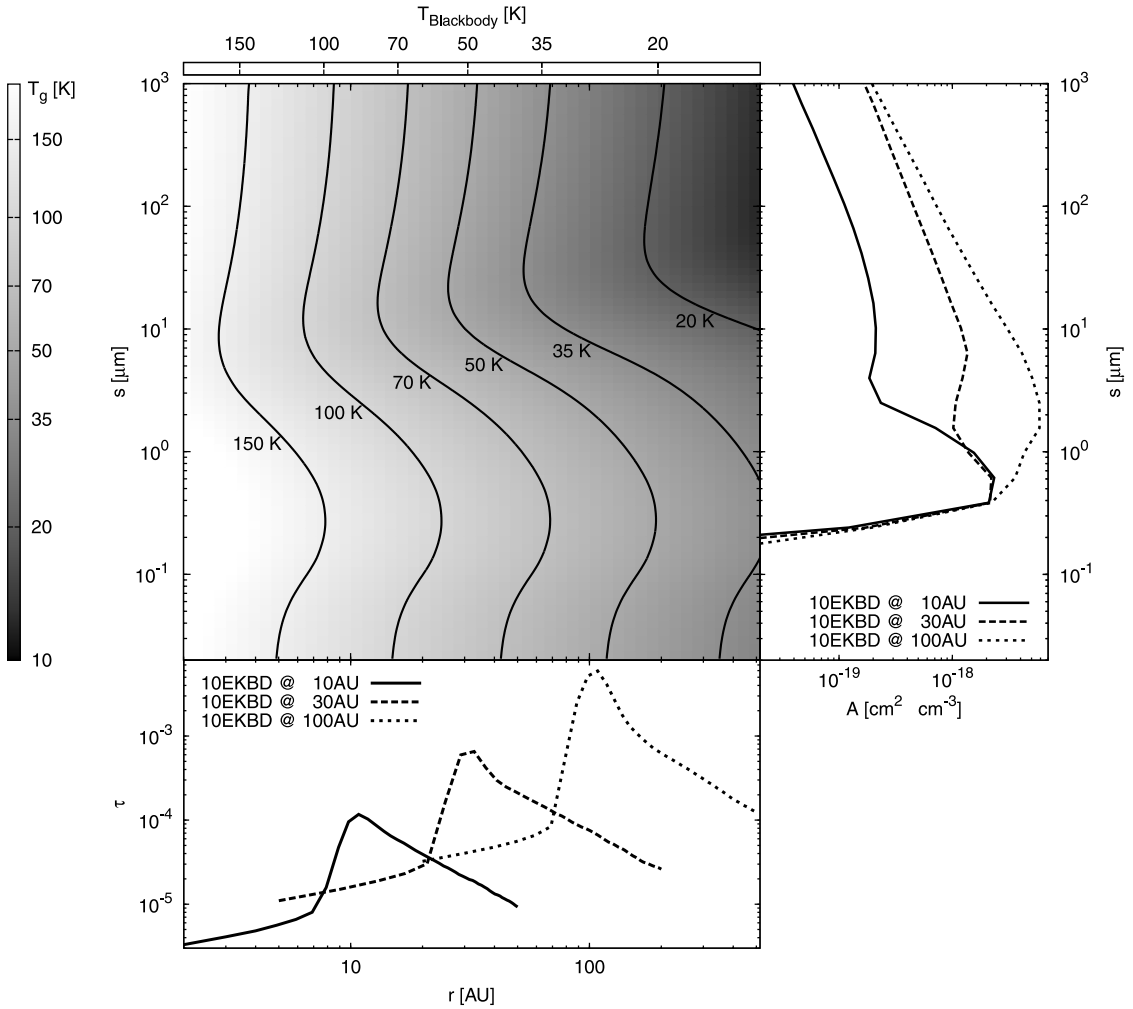

FIG. 6.—*Top left*: Equilibrium temperature of dust particles as a function of their distance from the star (*horizontal axis*) and size (*vertical axis*). Contours are isotherms. The blackbody dust temperatures are given along the upper edge of the plot for comparison. *Right*: Size distribution at the "central" distance of the systems (10 AU, *solid line*; 30 AU, *dashed line*; and 100 AU, *dotted line*) at 100 Myr. *Bottom left*: Normal optical depth for the same three disks as a function of distance to the star. An intersection of a horizontal straight line going through the maximum of the size distribution in a disk (*right*) with a vertical line through the peak of its radial profile (*bottom*) provides the typical dust temperature in that disk.

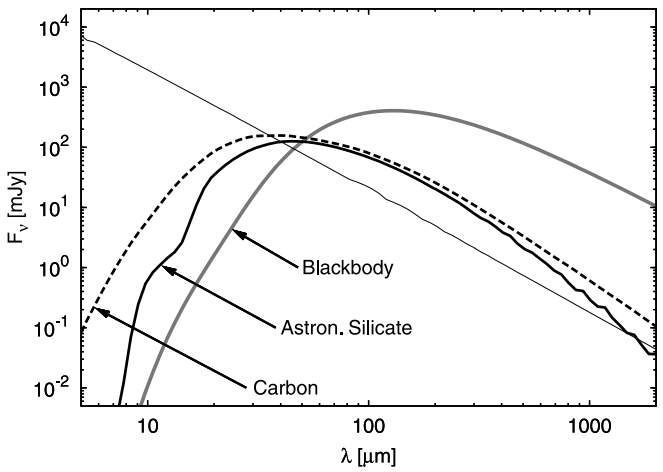

FIG. 7.—Emission from the same 1EKBD at 30 AU at 100 Myr disk, calculated under different assumptions about absorbing and emitting properties of dust grains: blackbody, astrosil (our nominal case), and amorphous carbon particles. The thin solid line shows the photosphere of a G2 V star.

that the difference applies only to the calculation of thermal emission. In other words, the dynamical modeling was still done by assuming the radiation pressure of astrosil and not of perfectly absorbing or carbon particles, but we assumed the grains to absorb and emit like a blackbody or carbon when calculating the thermal emission. There is a striking difference between the curves, especially the blackbody SED deviates from the others dramatically. The blackbody assumption leads to a strong increase of the total flux as well as to a shift of the maximum in the SED from 50 to 130 μm! In addition the excess drops toward longer wavelengths much slower than in the case of the astronomical silicate. In fact, it will never intersect the stellar photospheric flux.

We now proceed with a set of SEDs for our grid of reference disks. Some of them are shown in Figure 8. The main features of these plots reveal no surprises. The absolute level of excess emission is higher for more massive disks, as well as for distant ones (which is just the consequence of the assumed "same-density" scaling, as described in § 3.5; see also Fig. 5). The amount of dust emission is roughly comparable with the photospheric emission for the midaged 1EKBD at 30 AU disk. This is consistent with the known fact that a several gigayear old EKB counterpart would only slightly enhance the photospheric emission even at the "best" wavelengths. The position of the maximum emission ranges from $\approx$30 μm for the 10 AU disk to $\approx$70 μm for the 100 AU disk. Note that blackbody calculation would predict the emission to peak at longer wavelengths; beyond 100 μm for a 100 AU disk.

Again, the hump seen in all SEDs slightly below 10 μm is due to a silicate feature in $Q_{\rm abs}$; furthermore, some traces of the second feature at 20 μm are barely visible. This explanation is supported by Figure 2, which shows the absorption efficiency feature in this spectral range for small particles. This becomes even more obvious by comparing the contribution of the different grain size decades. For 0.1–1 μm particles the hump is more pronounced than for larger ones (see Fig. 9, *left*), as is the case for the absorption efficiency. Further on, the 10 μm "excess" becomes less visible for most distant disks (Fig. 8, *top to bottom*), where the average temperatures are lower, the maximum emission shifts to longer wavelengths, and therefore the Planck curve at $\lambda \sim 10$–20 μm is steeper.

The left panels in Figure 9 illustrate relative contributions of different-sized particles to the full SEDs. This is useful to get an idea which instrument is sensitive to which grain sizes. The blowout grains with radii less than 0.4 μm make only modest contribution to the flux even at 10 μm. The mid-IR fluxes are always dominated by bound grains with 0.4–1 μm radii (for the 10 and 30 AU rings) or those with 0.4–10 μm (for the 100 AU ring). In the far-IR, particles up to 100 μm in size play a role. The greatest effect on the submillimeter fluxes is that of 100 μm to 1 mm grains.

The position of the different maxima in Figure 9 can be understood by comparing the size decades to the dust temperature plot (Fig. 6). Particles of 0.1–1 μm are on the average a bit warmer than particles of 1–10 μm. However, the size distribution shows that the second decade is dominated by particles only slightly larger than 1 μm, which are still nearly as warm as the particles in the decade below. Thus, the maxima of the corresponding SED contributions are shifted only slightly. It is the step to the next decade where the decrease of temperature becomes very obvious by a large shift of the maximum. From that size on, the maxima stay nearly at the same position (in fact the maxima are shifted again to smaller wavelengths) as the temperature changes only marginally.

Similar to the contribution of the different size decades in the left panel, the right panels in Figure 9 demonstrate the contribution of the different radial parts of the disk to the total SED. As expected, most of the flux comes from the medium distances as this is the location of the birth ring. The second largest contribution is made by the outer part of the ring.

5. APPLICATION TO SELECTED DEBRIS DISKS

5.1. *Measured Fluxes*

To test the plausibility of our models, we have selected several nearby Sun-like stars known to possess debris dust. We used published data sets to search for stars with (1) spectral classes most likely G2 V (or very close), and (2) unambiguous excesses probed in a wide range of wavelengths from near-IR to far-IR or submillimeter. The resulting five stars and their properties are listed in Table 2, a summary of observational data on them is given in Table 3, and the disk properties as derived in original papers are collected in Table 4. The data include those from various surveys with *IRAS*, *ISO*, *Spitzer*, Keck II, and JCMT (Table 3). The estimated ages of the systems range from 30 to 400 Myr (Table 2) and the fractional luminosities from $\sim 10^{-5}$ to $\sim 10^{-3}$ (Table 4). The collected data points for our sample stars (photosphere + dust) are plotted in Figure 10.

5.2. *Observed Excesses*

Symbols in Figure 11 represent the observed excess emission for our sample stars. In the cases where the photospheric subtraction was done in the source papers, we just used the published data points. In the cases where only the total measured flux (star + dust) was given, we proceeded as follows. Three IRAC points (3.6, 4.5, and 8.0 μm) were fitted by an appropriate NextGen model (Hauschildt et al. 1999), and the resulting photospheric spectrum was subtracted from the fluxes measured at longer wavelengths. As far as the data quality is concerned, the best case is clearly HD 107146, where the data points cover a broad range between 10 μm and 1 mm. In other cases, the longest wavelengths probed lay at 70–160 μm. As a result, it is sometimes unclear where exactly the excess peaks. This is exemplified by HD 70573, where the 160 μm point has a huge error bar.

Yet before any comparison with the modeled SEDs, the resulting points in Figure 11 allow several quick conclusions. Notwithstanding the paucity of long-wavelength data just discussed, in all five systems the excess seems to peak at or slightly beyond

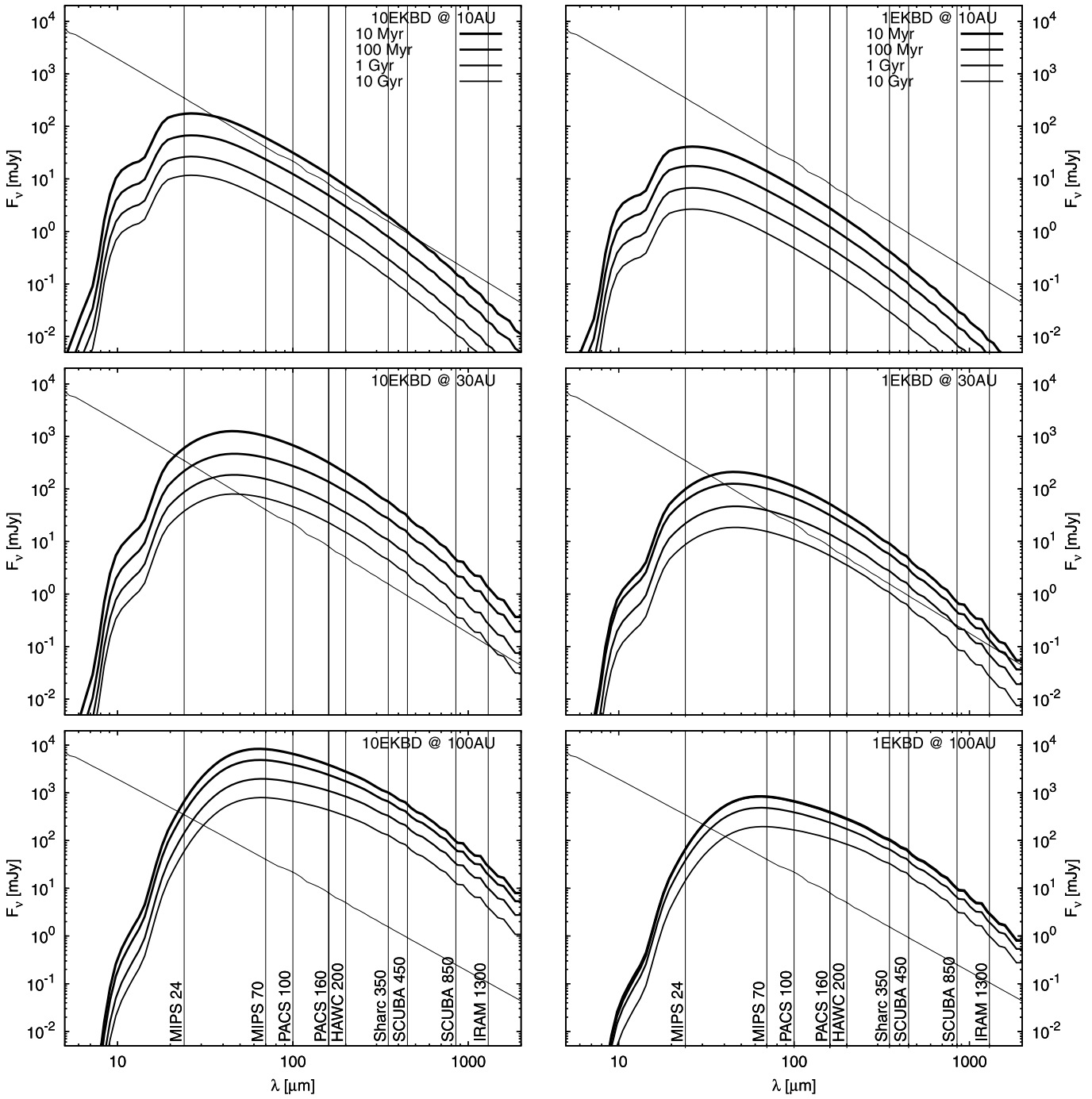

FIG. 8.—SEDs of disks stemming from planetesimal rings with different masses at different locations and at different time steps. To obtain the absolute values of fluxes, a distance of 10 pc was assumed. *Left*: Reference disks (10EKBD). *Right*: Less massive disks (1EKBD). The results for the latter have been obtained with the aid of eq. (4). *Top to bottom*: SEDs of the simulated planetesimal rings at 10, 30 and 100 AU. In each panel, lines of decreasing thickness correspond to the ages of 10 Myr, 100 Myr, 1 Gyr, and 10 Gyr. Note that the evolution of the 1EKBD at 100 AU disk at the beginning is very slow, so that the SEDs at 10 and 100 Myr are indistinguishable. Vertical lines indicate centers of observational bands of several instruments (in μm): *Spitzer* MIPS (24, 70, and 160), *Herschel* PACS (100 and 160), SOFIA HAWC (200), CSO Sharc (350), JCMT SCUBA/SCUBA 2 (450 and 850), and MPIfR IRAM (1300). A thin line from top left to bottom right is the stellar photosphere.

100 μm, suggesting a "cold EKB" as a source of dust. In addition, in all systems except for HD 377, a warm emission at $\lambda <$ 20 μm seems to be present, implying a closer-in "asteroid belt."

5.3. *Comparison of Measured and Modeled SEDs*

We now proceed with a comparison between the observed dust emission and the modeled emission. We stress that our goal here is *not* to provide the *best* fit to the observations possible with our approach, but rather to demonstrate that a set of reference disks modeled in the previous sections can be used to make rough preliminary conclusions about the planetesimal families.

To make such a comparison, we employ the following procedure:

1. For each star, we first look whether only cold or cold + warm excess emission is present. In the former case (HD 377), we fit the data points with a single "cold" reference disk. In the latter case (all other systems), we invoke a two-component model: a close-in 3 AU disk and an appropriate cold disk.

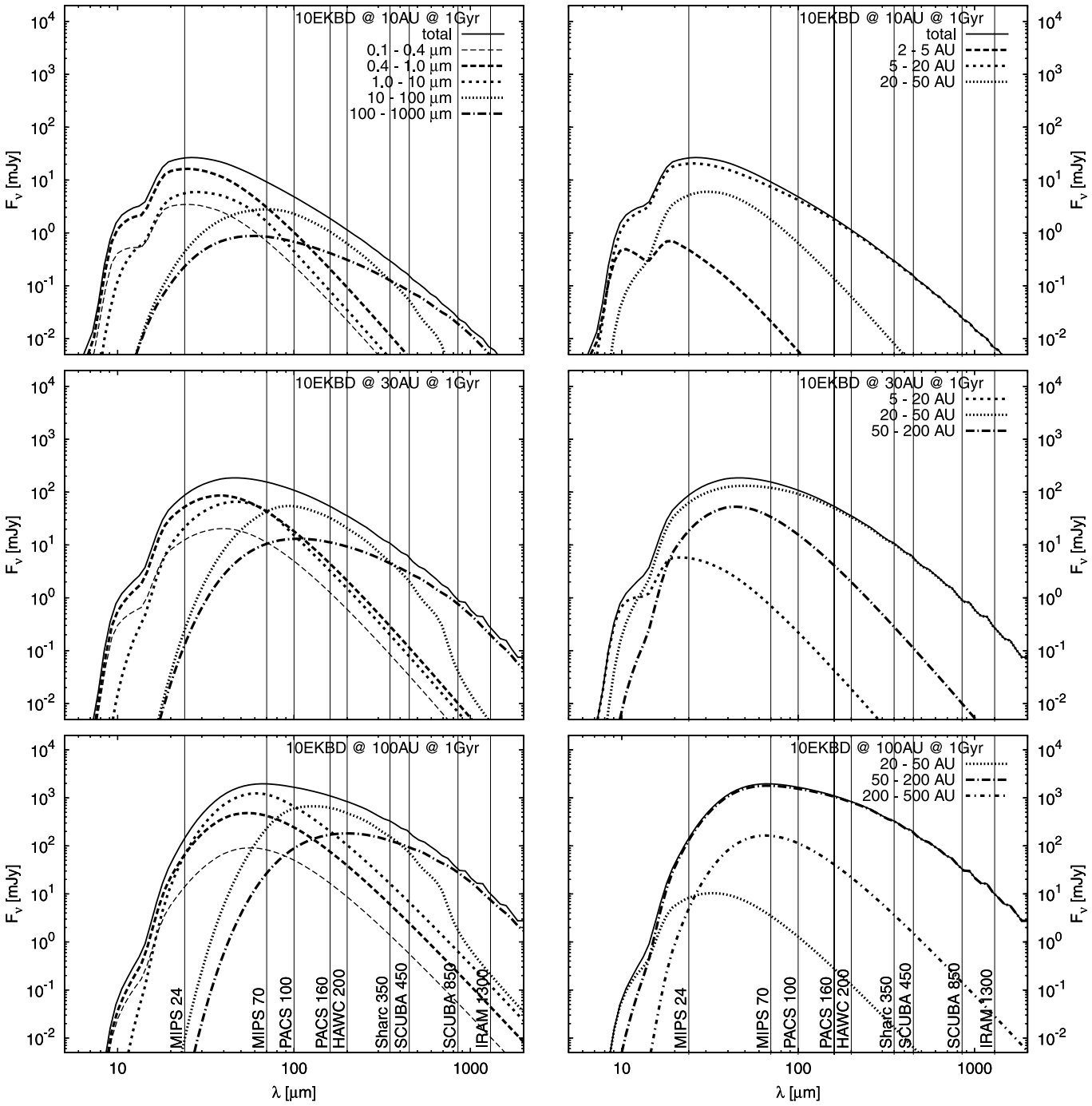

FIG. 9.—Contribution of individual grain size decades (shown with different linestyles in the left panels) and individual radial annuli of the disks (shown with different linestyles in the right panels) to the SED. As the grain blowout radius is $\approx 0.4\ \mu$m (see Fig. 1) in the left panels we split the lowest size decade into blowout grains with $s \in [0.1\ \mu\text{m}, 0.4\ \mu\text{m}]$ and bound ones with $s \in [0.4\ \mu\text{m}, 1.0\ \mu\text{m}]$. Panels from top to bottom correspond to planetesimal rings at 10, 30, and 100 AU. The initial density of all disks is 10EKBD and their age is 1 Gyr.

2. The location of the cold planetesimal belt is chosen according to the peak wavelength of the measured excess: 100 AU (HD 72905 and HD 141943) or 200 AU (HD 377, HD 70573, and HD 107146).

3. We then scale each of the two reference SEDs, warm and cold (or only one for HD 377), vertically to come to the observed absolute flux. Physically, it necessitates a change in the initial disk mass. However, it is *not* sufficient to change the initial disk mass by the ratio of the observed flux and the flux from a reference disk. The reason is that a change in the initial mass also alters the rate of the collisional evolution, whereas we need the "right" flux at a fixed time instant, namely, the actual age of the system (Table 2). Therefore, to find the mass modification factor we apply scaling rules, as explained in Appendix A. Specifically, we solve equation (A8). In the systems that reveal both warm and cold emission, this is done separately for the inner and outer disk.

The results presented in Figure 11 with lines show that the modeled SEDs can, generally, reproduce the data points within their error bars. Again, the judgment should take into account the fact that we are just using one or two pregenerated SEDs for

TABLE 2
Stellar Parameters

Star	$T_{\rm eff}$ (K)	$\log L_*/L_\odot$	D (pc)	Age (Myr)
HD 377	5852[a]	0.09[a]	40[a]	32[a]
HD 70573	5841[a]	−0.23[a]	46[a]	100[a]
HD 72905[b]	5831[a]	−0.04[a]	13.85[c]	420[c]
HD 107146	5859[a]	0.04[a]	29[a]	100^{+100}_{-20}[d]
HD 141943	5805[a]	0.43[a]	67[a]	32[a]

[a] From Hillenbrand et al. (2008).
[b] A G1.5 star.
[c] From Trilling et al. (2008).
[d] From Moór et al. (2006).

TABLE 3
Observational Data for the Five G2 Stars and Their Disks

Star	Instrument, λ (μm)	Reference
HD 377	IRAC 3.6/4.5/8.0	Hillenbrand et al. (2008)
	IRAS 13/33	Hillenbrand et al. (2008)
	IRAS 60	Moór et al. (2006)
	MIPS 24/70/160	Hillenbrand et al. (2008)
HD 70573[a]	IRAC 3.6/4.5/8.0	Hillenbrand et al. (2008)
	IRS 13/33	Hillenbrand et al. (2008)
	MIPS 24/70/160	Hillenbrand et al. (2008)
HD 72905	IRAC 3.6/4.5/8.0	Hillenbrand et al. (2008)
	IRS 13/33	Beichman et al. (2006)
	IRAS 12/25	Spangler et al. (2001)
	ISOPHOT 60/90	Spangler et al. (2001)
	MIPS 24	Bryden et al. (2006)
	MIPS 70	Hillenbrand et al. (2008)
HD 107146[b]	IRAC 3.6/4.5/8.0	Hillenbrand et al. (2008)
	LWS 11.7/17.8	Metchev et al. (2004)
	IRS 13/33	Hillenbrand et al. (2008)
	IRAS 60/100	Moór et al. (2006)
	MIPS 24/70	Hillenbrand et al. (2008)
	SCUBA 450/850	Williams et al. (2004)
HD 141943	IRAC 3.6/4.5/8.0	Hillenbrand et al. (2008)
	IRS 13/33	Hillenbrand et al. (2008)
	MIPS 24/70	Hillenbrand et al. (2008)

[a] A planet host star (Setiawan et al. 2007).
[b] Resolved in *V* and *I* bands (Ardila et al. 2004), at 350 and 450 μm (Williams et al. 2004), and at 3 mm (Carpenter et al. 2005).

a rather coarse grid of reference disks. Much better fits would certainly be possible if we allowed a more exact positioning of parent belts and let additional model parameters vary. Dust opacities, initial distributions of planetesimals' sizes and orbital elements, as well as their mechanical properties that were fixed in modeling of the collisional outcomes would all be at our disposal for this purpose. Furthermore, more than two-component planetesimal belts could be astrophysically relevant as well, as is the case in our solar system (asteroid belt, different cometary families, and various populations in the EKB).

We now come to the interpretation of the fitting results, trying to recover the properties of dust-producing planetesimal belts. Table 5 lists them for all systems. The most important information is the deduced mass and location of the belts.

5.4. *Results for Hot Dust*

As far as the hot dust components in four out of five systems are concerned, our results show that these can be explained by "massive asteroid belts" with roughly the lunar mass in bodies up to ∼100 km in size, located at 3 AU, with a width of ∼1 AU. However, the quoted distance of inner components—3 AU—is only due to the fact that this is the smallest disk in our grid. This distance can only be considered as an upper limit: the SEDs seem perfectly compatible with disks as far in as 0.3 AU, as suggested for the case of HD 72905 (Wyatt et al. 2007).

What is more, even the very fact that hot excess is real can sometimes be questioned, since it can be mimicked by photospheric emission slightly larger than the assumed values. Indeed, the excess for HD 70573 and HD 72905 at wavelengths around and below 25 μm does not exceed 10%, which is comparable with the average calibration uncertainty and therefore has to be considered marginal (Bryden et al. 2006; Hillenbrand et al. 2008). Only in the case of HD 72905, the *Spitzer* IRS detection of the 10 μm emission from hot silicates provides an independent confirmation that the hot excess is real (Beichman et al. 2006). However, the HD 72905 plot in Figure 11 makes it obvious that some problems occurred in terms of the photosphere fitting. All data points that we obtained by subtracting the IRAC photospheric fluxes (*squares*) systematically lie above the data points where a photosphere from the literature was subtracted (*circles*). The origin of the difference is unclear; on any account, the problem cannot be mitigated by the assumption that an excess is already present at IRAC wavelengths, since this would shift the squares further upwards. Considering the circles to be more trustworthy, the shape of the SED to fit changes. Then a closer-in disk at ∼0.3 AU could better reproduce the fluxes in the near- and mid-infrared, while the outer ring would have to be shifted to a distance somewhat larger than 100 AU in order not to surpass the measured flux at 33 μm. A problem would arise with the inner disk: at ∼0.3 AU, the collisional evolution is so rapid that an unrealistically large initial belt mass would be necessary. Similar arguments have led Wyatt et al. (2007) to the conclusion that HD 72905 must be a system at a transient phase rather than a system collisionally evolving in a steady state.

Still, treating the derived sizes and masses of the inner disks as upper limits yields physical implications. Because the collisional evolution close to the star is rapid, such belts must have lost up to two-thirds of their initial mass before they have reached their present age (cf. initial and current mass in Table 5). In the case of HD 70573, the known giant planet with $a = 1.76$ AU and $e = 0.4$ (Setiawan et al. 2007) does not seem to exclude the existence of a dynamically stable planetesimal belt either inside ∼1 AU or outside ∼3 AU.

5.5. *Results for Cold Dust*

The estimated parameters of the outer components of the disks suggest "massive and large Kuiper Belts." The radii of the outer rings are larger than the radii derived in previous studies (cf. Tables 4 and 5). This traces back to our using astrosilicate instead of blackbody when calculating the dust emission, so that the same dust temperatures are attained at larger distances (see Fig. 7).

Since one disk in our sample, that of HD 107146, has been resolved, it is natural to compare our derived disk radius with the one obtained from the images. Williams et al. (2004) report an outer border of the system of 150 AU based on submillimeter images. In contrast, Ardila et al. (2004) detected an 85 AU wide ring peaking in density at about 130 AU. This is comparable to, although somewhat smaller than, our 200 AU radius. However, moving the outer ring to smaller distances would increase the fluxes in the mid infrared where the SED already surpasses the observations and the other way round in the submillimeter region.

TABLE 4
PREVIOUSLY DERIVED DISK PROPERTIES

Star	T_{dust} (K)	R_{dust} (AU)	M_{dust} ($M_\oplus$)	L_{dust}/L_*
HD 377	58[a,b]	23[a,c]	3.98×10^{-4}[a,d]	3.98×10^{-4}[a,e]
				$(4.0 \pm 0.3) \times 10^{-4}$[f,g]
HD 70573	41[a,b]	35[a,c]	2.0×10^{-5}[a,d]	1.0×10^{-4}[a,e]
HD 72905	103[a,b]	7[a,c]	1.58×10^{-6}[a,d]	2.0×10^{-5}[a,e]
	63–67[h,i]	12.2–15.9[h,i]	3.3×10^{-6}[h,i]	2.9×10^{-5}[h,j]
	123[k,l]	6.2[c,k]		$(0.6–1.5) \times 10^{-5}$[k,m]
				1.6×10^{-5}[n,o]
				2.8×10^{-4}[k,p]
HD 107146	52[a,b]	30[a,c]	1.26×10^{-3}[a,d]	4.94×10^{-4}[a,e]
		13.6– > 200[a,q]		
			3.2×10^{-7}[r,s]	$(9.2 \pm 0.9) \times 10^{-4}$[f,g]
	55[l,t]	29[c,t]	8.99×10^{-2}[t,u]	9.5×10^{-4}[g,t]
	51[v,w]	>31–150[v,x]	0.1[v,w]	1.2×10^{-3}[v]
HD 141943	85[a,b]	18[a,c]	7.94×10^{-5}[a,d]	1.58×10^{-4}[a,e]
		8.6–40[a,q]		

[a] From Hillenbrand et al. (2008).
[b] Color temperature (33–70 μm) from blackbody SED fitting.
[c] Derived from T_{dust} assuming blackbody (lower limit).
[d] Derived from fractional luminosity for an average grain size of $\langle a \rangle = 10$ μm and a density of $\rho = 2.5$ g cm^{-3}.
[e] Derived from T_{dust} and R_{dust} using the Stefan-Boltzmann relation.
[f] From Moór et al. (2006).
[g] $L_{dust}/L_* = L_{IR}/L_{bol}$.
[h] From Beichman et al. (2006).
[i] From SED fitting using 10 μm silicate grains with a temperature profile following a power law (favored model in Beichman et al. 2006).
[j] L_{dust} obtained by integrating IRS spectrum (10–34 μm) after extrapolation to 70 μm.
[k] From Spangler et al. (2001).
[l] From SED fitting using a single temperature blackbody.
[m] L_{dust} is derived from the SED fitting, and L_* is obtained by integrating the corresponding Kurucz model.
[n] From Bryden et al. (2006).
[o] Minimum value, derived from the 70 μm measurement.
[p] L_* is the stellar bolometric luminosity, and L_{dust} is the sum of the luminosities in each (*IRAS*) wavelength band with a correction (for longer wavelengths).
[q] Extended ring derived from blackbody SED fitting assuming a constant surface density.
[r] From Carpenter et al. (2005).
[s] Derived for $T_{dust} = 40$ K using a frequency-dependent mass absorption coefficient.
[t] From Rhee et al. (2007).
[u] Derived from submillimeter observations using a dust opacity of 1.7 cm^2 g^{-1} at 850 μm.
[v] From Williams et al. (2004).
[w] From single-temperature SED fitting using a modified blackbody and a mass absorption coefficient $\kappa_{850} =$ 1.7 cm^2 g^{-1}.
[x] Inner border derived from SED fitting, outer border taken from resolved image.

The resulting deficiency of submillimeter fluxes, however, could be due to roughness of Mie calculations. As pointed out by Stognienko et al. (1995), an assumption of homogeneous particles typically leads to underestimation of the amount of thermal radiation in the submillimeter region.

Large belt radii imply large masses. Dust masses derived here are by 2 orders of magnitude larger than previous estimates (cf. Tables 5 and 4). The total masses of the belts we derive range from several to several tens of Earth masses, to be compared with $\sim 0.1\ M_\oplus$ in the present-day EKB (although there is no unanimity on that point—cf. Stern & Colwell 1997). Note that, as the collisional evolution at 100–200 AU is quite slow, whereas the oldest system in our sample is only 420 Myr old, the difference between the initial disk mass and the current disk mass is negligible. Assuming several times the minimum mass solar nebula with a standard surface density of solids $\Sigma \sim 50\ \mathrm{g\ cm^2} (r/1\ \mathrm{AU})^{-3/2}$ (e.g., Hayashi et al. 1985), the mass of solids in the EKB region would be a few tens of Earth masses; and current models (e.g., Kenyon & Luu 1999b) successfully accumulate 100 km sized EKB objects in tens of Myr. However, it is questionable whether the assumed radial surface density profile could extend much farther out from the star. As a result, it is difficult to say whether a progenitor disk could contain enough solids as far as at 200 AU from the star to form a belt of 30–50 $M_\oplus$.

However, such questions may be somewhat premature. On the observational side, more data are needed, especially at longer wavelengths; for instance, the anticipated *Herschel* data (PACS at 100/160 μm and SPIRE at 250–500 μm) would help a lot. On the modeling side, a more systematic study is needed to clarify, how strongly various assumptions of the current model (especially the collisional outcome prescription and the material choices) may affect the calculated size distributions of dust, the dust grain temperatures, and the amount of their thermal emission.

At this point, we can only state that in the five systems analyzed (with a possible exception of HD 72905) and with the caveat that available data are quite scarce, the observations are not incompatible with a standard steady-state scenario of collisional evolution and dust production. Of course, other possibilities, such as major collisional breakups (Kenyon & Bromley 2005; Grigorieva et al. 2007) or events similar to the late heavy bombardment (as

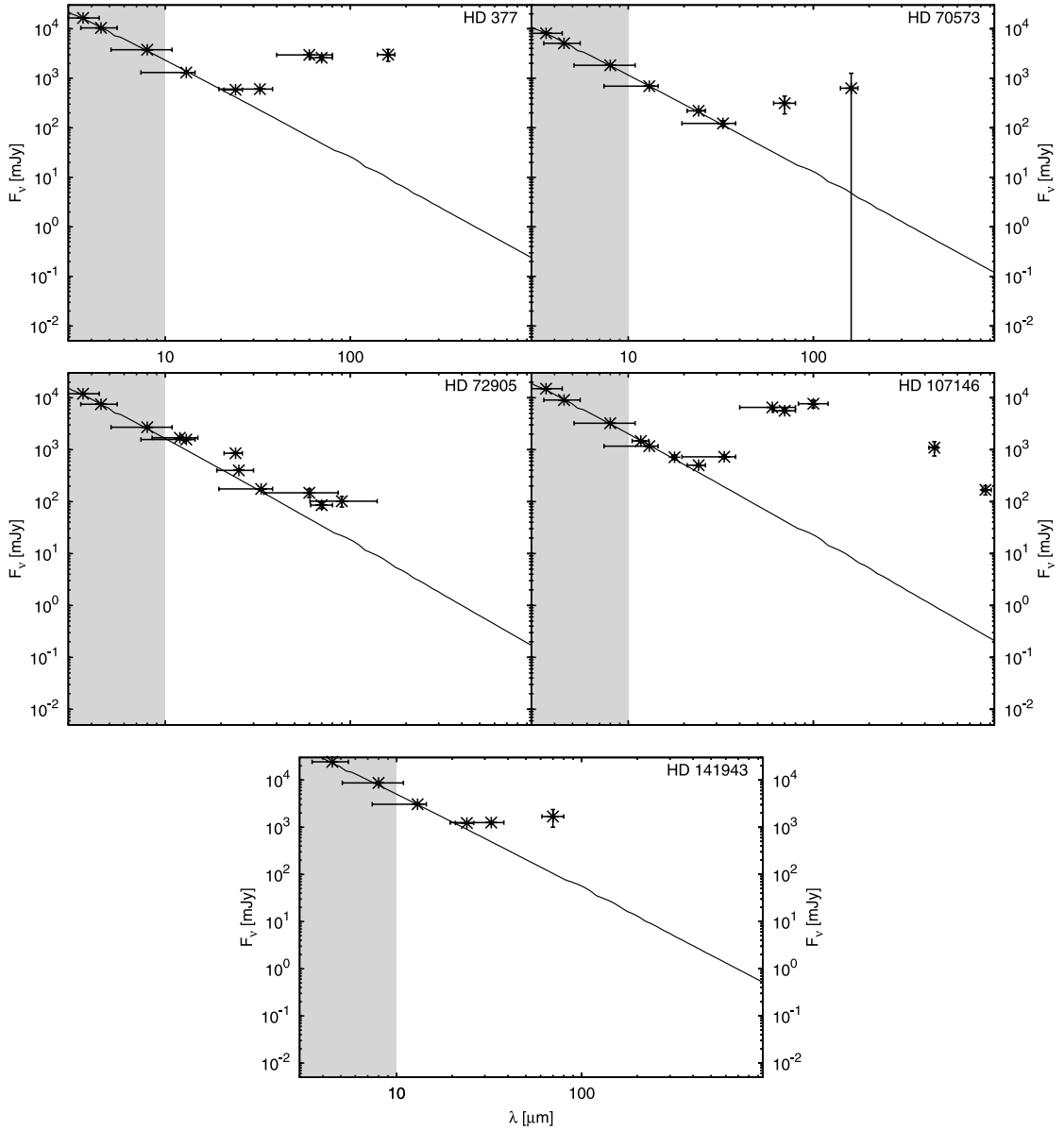

FIG. 10.—Observational data for five selected G2 V stars. Note that all fluxes have been scaled to the same standard distance of 10 pc. Symbols in the left-hand, gray-shaded part of each panel ($\lambda < 10$ μm) are IRAC observations. They are used to find an appropriate Hauschildt model to the photosphere (*thin solid line*), assuming that no excess is already present in the near infrared. Vertical error bars are 1 σ observational uncertainties, taken from the source papers. Horizontal bars indicate the bandwidth of the respective detector.

suggested, for instance, for HD 72905; Wyatt et al. 2007) cannot be ruled out for the inner disks.

6. SUMMARY

Debris disks around main-sequence stars may serve as tracers of planetesimal populations that have accumulated at earlier, protoplanetary and transitional, phases of systems' evolution, and have not been used up to form planets. However, observations of debris disks are only sensitive to the lowest end of the size distribution. Using dynamical and collisional models of debris disks is the only way to "climb up" the ladder of the collisional cascade, past the ubiquitous micron-sized grains toward parent bodies and toward the main mass reservoir of the disks.

The main idea of this paper has been to take a grid of planetesimal families (with different initial masses, distances from a central star, etc.), to collisionally "generate" debris disks from these families and evolve them with the aid of an elaborated collisional code, and finally to calculate SEDs for these disks. A comparison/fit of the observed SEDs with the pregenerated SEDs is meant to allow quick conclusions about the properties of the planetesimal belt(s) that maintain one or another observed disk.

Our specific results are as follows:

1. We have produced five reference disks around a G2 V star from planetesimal belts at 3, 10, 30, 100, and 200 AU with 10 times the EKB mass density and evolved them for 10 Gyr. With an appropriate scaling rule (eq. [A1]), we can translate these results to an arbitrary initial disk mass and any age between 10 Myr and 10 Gyr. Thus, we effectively have a three-parametric set of reference disks (initial mass, location of planetesimal belt, and age). For all the disks, we have generated SEDs, assuming astrosilicate (with tests made also for blackbody and amorphous carbon).

2. We have selected five G2 V stars with good data (*IRAS*; *ISO* ISOPHOT; *Spitzer* IRAC, IRS, MIPS; Keck II LWS; and JCMT SCUBA) and tested our grid against these data. For all five systems, we have reproduced the data points within the error bars

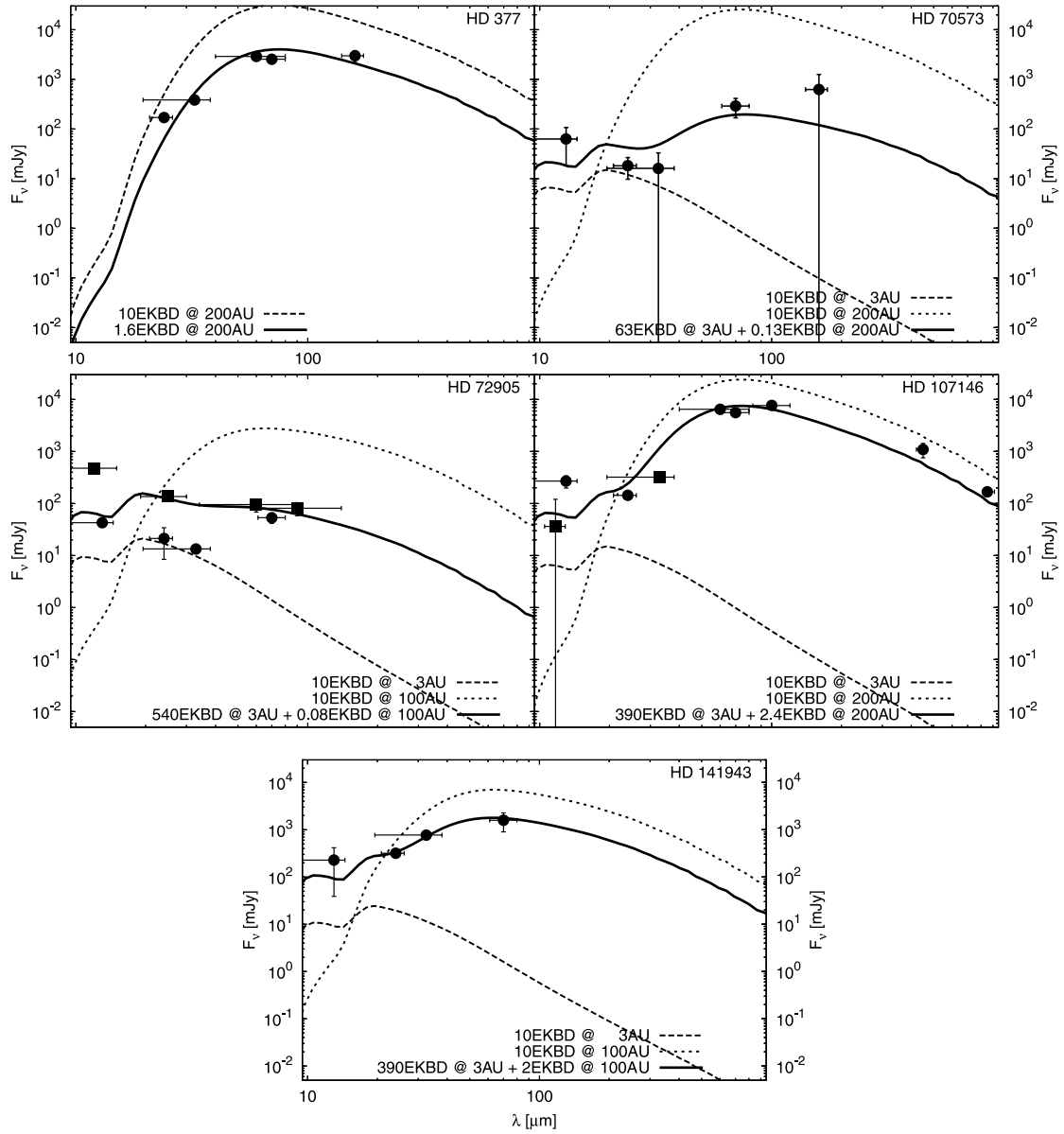

FIG. 11.—Observed (*symbols*) and modeled (*lines*) excess emission, scaled to a distance of 10 pc. The wavelength range matches the unshaded part of Fig. 10. Here, in contrast to Fig. 10, symbols represent the *excess* emission. Squares mark the cases where the scaled NextGen model shown on that figure was used to subtract the photosphere. Circles indicate that for these observations the stellar emission was subtracted using photospheric fluxes as given in the respective papers. *Dashed lines*: Two "underlying" SEDs of reference disks (unscaled, i.e., with 10EKBD), one for cold excess and one for warm excess (except for HD 377, where only the cold component is observed). *Solid line*: Linear combination of two scaled reference SEDs that provides a reasonable fit to the data points (except for HD 377, where a single scaled reference SED is sufficient).

with a linear combination of two disks from the grid (an "asteroid belt" at 3 AU and an outer "Kuiper Belt"). This automatically gives us the desired estimates of planetesimals (location, total mass, etc.).

3. A comparison of the observational data on the five stars with the grid of models leads us to a conclusion that the cold emission (with a maximum at the far-IR) is compatible with "large Kuiper Belts," with masses in the range 3–50 $M_\oplus$ and radii of 100–200 AU. These large sizes trace back to the facts that the collisional model predicts the observed emission to stem from micron-sized dust grains, whose temperatures are well in excess of a blackbody temperature at a given distance from the star (as discussed, e.g., in Hillenbrand et al. 2008). This conclusion is rather robust against variation in parameters of collisional and thermal emission models, and is roughly consistent with disk radii revealed in scattered light images (e.g., HD 107146). Still, quantitative conclusions about the mass and location of the planetesimal belts would significantly depend on (1) the adopted model of collision outcomes (which, in turn, depend on the dynamical excitation of the belts, i.e., on orbital eccentricities and inclinations of planetesimals) and (2) the assumed grains' absorption and emission efficiencies. For example, a less efficient cratering (retaining more grains with radii $\sim$10 μm in the disk) and/or more "transparent" materials (making dust grains of the same sizes at the same locations colder) would result in "shifting" the parent belts closer to the star.

In future, we plan to extend this study in two directions. First, we will investigate more systematically the influence of the dust composition by trying relevant materials with available optical data rather than astrosilicate; this should be done consistently in the dynamical/collisional and thermal emission models. Second,

TABLE 5
Disk Properties Derived in this Study

Star	Component	$M_{\rm disk}$[a] ($M_\oplus$)	$R_{\rm belt}$[b] (AU)	$M_{\rm dust}$[c] ($M_\oplus$)	$T_{\rm dust}$[d] (K)
HD 377	Outer	(32) 32	200	3.1×10^{-2}	40
HD 70573	Inner	(0.0063) 0.0046	3	1.4×10^{-7}	200
	Outer	(2.6) 2.5	200	2.0×10^{-3}	40
HD 72905	Inner	(0.054) 0.019	3	3.4×10^{-8}	200
	Outer	(0.23) 0.23	100	2.1×10^{-4}	50
HD 107146	Inner	(0.039) 0.023	3	4.9×10^{-7}	200
	Outer	(47) 47	200	4.8×10^{-2}	40
HD 141943	Inner	(0.039) 0.027	3	8.0×10^{-7}	200
	Outer	(6.1) 6.1	100	5.5×10^{-3}	50

[a] Initial mass (in parentheses) and the current mass of the whole planetesimal disk (bodies up to 100 km in radius).
[b] Location of the parent planetesimal belt.
[c] Current mass of "visible" dust (grains up to 1 mm in radius).
[d] Temperature of cross section–dominating astrosil grains at the location of the parent planetesimal belt; see explanation in Fig. 6.

it is planned to extend this study to stars with a range of spectral classes. This will result in a catalog of disk colors that should be helpful for interpretation of data expected to come, most notably from the *Herschel Space Observatory*.

This work has been particularly motivated by the Herschel Open Time Key Program "DUNES" (DUst around NEarby Stars; PI: C.Eiroa), and we wish to thank many colleagues involved in DUNES (in particular, Jean-Charles Augereau, Jens Rodmann, and Philippe Thébault) for encouragement and numerous discussions. A speedy and constructive review of an anonymous reviewer helped to improve the paper. This research has been funded by the Deutsche Forschungsgemeinschaft (DFG), projects Kr 2164/5-1 and Mu 1164/6-1, by the Deutscher Akademischer Austauschdienst (DAAD), project D/0707543, and by the International Space Science Institute (Bern).

APPENDIX A

SCALING RULES

Rule 1: Dependence of evolution on initial disk mass.—Consider a disk with initial mass $M(t=0)\equiv M_0$ at a distance r from the star with age t. Denote by $F(M_0,r,t)$ any quantity directly proportional to the amount of disk material in any size regime, from dust grains to planetesimals. In other words, F may equally stand for the total disk mass, the mass of dust, its total cross section, etc. As found by Löhne et al. (2008) there is a scaling rule,

$$F(xM_0,r,t)=xF(M_0,r,xt), \tag{A1}$$

valid for any factor $x>0$. This scaling is an *exact* property of every disk of particles, provided these are produced, modified and lost in binary collisions and not in any other physical processes.

Rule 2. Dependence of evolution on distance.—Another scaling rule is the dependence of the evolution timescale on the distance from the star (Wyatt et al. 2007; Löhne et al. 2008). Then

$$F(M_0,xr,t)\approx F(M_0,r,x^{-4.3}t). \tag{A2}$$

Unlike equation (A1), this scaling is approximate.

Rule 3. Dust mass as a function of time.—Finally, the third scaling rule found in Löhne et al. (2008) is the power-law decay of the dust mass

$$F(M_0,r,xt)\approx x^{-\xi}F(M_0,r,t), \tag{A3}$$

where $\xi\approx 0.3\ldots0.4$ (Fig. 12). This scaling is also approximate and, unlike equations (A1) and (A2), only applies to every quantity directly proportional to the amount of *dust*. In this context, "dust" refers to all objects in the strength rather than gravity regime, implying radii less than about 100 m. The scaling is sufficiently accurate for disks that are much older than the collisional lifetime of these 100 m sized bodies. This is also seen in Figure 12: while for the 3 AU disk the power law (eq. [A3]) sets in after $\ll$1 Myr, the 200 AU disk needs $\sim$100 Myr to reach this regime.

Note that the "pre-steady-state" phase of collisional evolution may actually require a more sophisticated treatment. Our runs assume initially a power-law size distribution of planetesimals, and an instantaneous start of the collisional cascade at $t=0$. In reality, an initial size distribution is set up by the accretion history of planetesimals and will surely deviate from a single power law. Moreover, at a certain phase cratering and destruction of objects may increasingly come into play simultaneously with ceasing, yet ongoing accretion; the

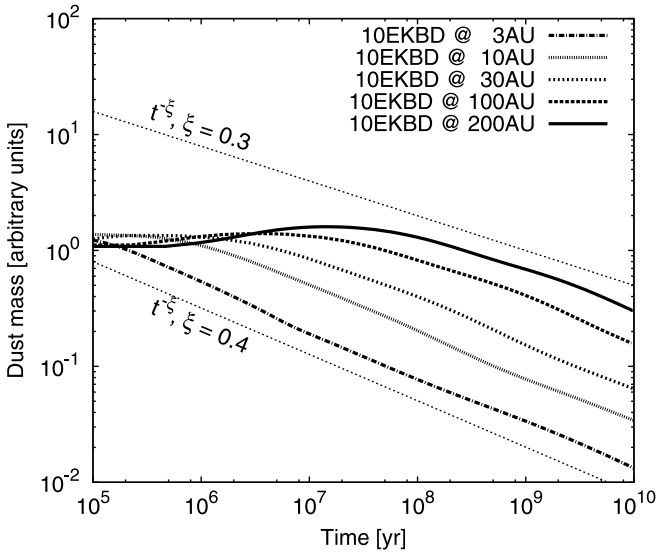

FIG. 12.—Time evolution of dust mass ($s < 1$ mm) for our five reference disks (*thick lines*). For comparison, power laws $t^{-\xi}$ with $\xi = 0.3$ and 0.4 are shown with thin dashed lines.

efficiencies and timescales of these processes will be different for different size ranges and different spatial locales in the disk (e.g., Davis & Farinella 1997; Kenyon & Luu 1998, 1999a, 1999b).

The usefulness of these scaling rules can be illustrated with the following examples.

Example 1.—Assuming now F to be the total amount of dust, from equations (A1)–(A3) one finds

$$F(xM_0, yr, t) \approx x^{1-\xi} y^{4.3\xi} F(M_0, r, t). \tag{A4}$$

Our choice of reference disks (different distances, but the same volume density) implies $x = y^3$. The normal optical optical depth $\tau \propto F/r^2$ scales as

$$\tau(y^3 M_0, yr, t) \approx y^{1+1.3\xi} \tau(M_0, r, t). \tag{A5}$$

Therefore, once a steady state is reached ($\xi \approx 0.3 \ldots 0.4$), a y times more distant planetesimal belt gives rise to a $y^{1+1.3\xi}$ times optically thicker disk. This explains, in particular, why in Figure 4 any 100 AU ring is ≈30 times optically thicker than the coeval 10 AU one.

Example 2.—Since the distance r in equations (A1) and (A3) is kept fixed, F in these equations can also denote the radiation flux, emitted by a disk at a certain wavelength. Let $F_o(t)$ be the observed flux from a disk of age t. Imagine a model of a disk of the same age with an initial mass M_0 predicts a flux $F(M_0, t)$ which is by a factor A lower than the observed one:

$$F_o(t) = AF(M_0, r, t). \tag{A6}$$

Our goal is to find the "right" initial mass, i.e., a factor B such that

$$F_o(t) = F(BM_0, r, t). \tag{A7}$$

With the aid of equation (A1), this can be rewritten as

$$F_o(t) = BF(M_0, r, Bt). \tag{A8}$$

Equation (A3) gives now

$$F_o(t) \approx BF(M_0, r, t) B^{-\xi} = B^{1-\xi} F(M_0, r, t), \tag{A9}$$

whence

$$B \approx A^{1/(1-\xi)}. \tag{A10}$$

For instance, a 10 times higher flux at a certain age requires a 27–46 times larger initial disk mass if $\xi = 0.3 \ldots 0.4$.

Although this rule is convenient for quick estimates, it should be used with caution. As described above, the value of ξ at the beginning of collisional evolution (which lasts up to 100 Myr for the 200 AU belt) can be much smaller—close to zero or even negative—than the "normal" $\xi = 0.3 \ldots 0.4$. For this reason, we prefer to use only the first scaling rule, equation (A1). Therefore, instead of applying equation (A10), we find B by solving equation (A8) numerically with a simple iterative routine. It is this way Figure 11 was constructed.

REFERENCES

Ardila, D. R., et al. 2004, ApJ, 617, L147
Artymowicz, P. 1997, Ann. Rev. Earth Planet. Sci., 25, 175
Aumann, H. H., et al. 1984, ApJ, 278, L23
Beichman, C. A., et al. 2005, ApJ, 622, 1160
———. 2006, ApJ, 639, 1166
Bohren, C. F., & Huffman, D. R. 1983, Absorption and Scattering of Light by Small Particles (New York: Wiley)
Bryden, G., et al. 2006, ApJ, 636, 1098
Burns, J. A., Lamy, P. L., & Soter, S. 1979, Icarus, 40, 1
Carpenter, J. M., Wolf, S., Schreyer, K., Launhardt, R., & Henning, T. 2005, AJ, 129, 1049
Davis, D. R., & Farinella, P. 1997, Icarus, 125, 50
Dohnanyi, J. S. 1969, J. Geophys. Res., 74, 2531
Durda, D. D., & Dermott, S. F. 1997, Icarus, 130, 140
Gladman, B., Kavelaars, J. J., Petit, J., Morbidelli, A., Holman, M. J., & Loredo, T. 2001, AJ, 122, 1051
Grigorieva, A., Artymowicz, P., & Thébault, P. 2007, A&A, 461, 537
Hahn, J. M., & Malhotra, R. 2005, AJ, 130, 2392
Hauschildt, P., Allard, F., & Baron, E. 1999, ApJ, 512, 377
Hayashi, C., Nakazawa, K., & Nakagawa, Y. 1985, in Protostars and Planets II, ed. D. C. Black & M. S. Matthews (Tucson: Univ. Arizona Press), 1100
Hillenbrand, L. A., et al. 2008, ApJ, 677, 630
Kenyon, S. J., & Bromley, B. C. 2005, AJ, 130, 269
Kenyon, S. J., & Luu, J. X. 1998, AJ, 115, 2136
———. 1999a, AJ, 118, 1101
———. 1999b, ApJ, 526, 465
Krivov, A. V., Löhne, T., & Sremčević, M. 2006, A&A, 455, 509
Krivov, A. V., Mann, I., & Krivova, N. A. 2000, A&A, 362, 1127
Krivov, A. V., Sremčević, M., & Spahn, F. 2005, Icarus, 174, 105
Laor, A., & Draine, B. T. 1993, ApJ, 402, 441
Löhne, T., Krivov, A. V., & Rodmann, J. 2008, ApJ, 673, 1123
Metchev, S. A., Hillenbrand, L. A., & Meyer, M. R. 2004, ApJ, 600, 435
Meyer, M. R., et al. 2004, ApJS, 154, 422
Moór, A., Ábrahám, P., Derekas, A., Kiss, C., Kiss, L. L., Apai, D., Grady, C., & Henning, T. 2006, ApJ, 644, 525
Najita, J., & Williams, J. P. 2005, ApJ, 635, 625
Rhee, J. H., Song, I., Zuckerman, B., & McElwain, M. 2007, ApJ, 660, 1556
Rieke, G. H., et al. 2005, ApJ, 620, 1010
Setiawan, J., Weise, P., Henning, T., Launhardt, R., Müller, A., & Rodmann, J. 2007, ApJ, 660, L145
Siegler, N., Muzerolle, J., Young, E. T., Rieke, G. H., Mamajek, E. E., Trilling, D. E., Gorlova, N., & Su, K. Y. L. 2007, ApJ, 654, 580
Spangler, C., Sargent, A. I., Silverstone, M. D., Becklin, E. E., & Zuckerman, B. 2001, ApJ, 555, 932
Stern, S. A., & Colwell, J. E. 1997, ApJ, 490, 879
Stognienko, R., Henning, T., & Ossenkopf, V. 1995, A&A, 296, 797
Su, K. Y. L., et al. 2006, ApJ, 653, 675
Thébault, P., & Augereau, J.-C. 2007, A&A, 472, 169
Thébault, P., Augereau, J.-C., & Beust, H. 2003, A&A, 408, 775
Trilling, D. E., et al. 2007, ApJ, 658, 1289
———. 2008, ApJ, 674, 1086
Williams, J. P., Najita, J., Liu, M. C., Bottinelli, S., Carpenter, J. M., Hillenbrand, L. A., Meyer, M. R., & Soderblom, D. R. 2004, ApJ, 604, 414
Wolf, S., & Hillenbrand, L. A. 2003, ApJ, 596, 603
Wyatt, M. C. 2005, A&A, 433, 1007
Wyatt, M. C., Smith, R., Greaves, J. S., Beichman, C. A., Bryden, G., & Lisse, C. M. 2007, ApJ, 658, 569